An Added-Mass Measurement Technique for Transducer Parameter Estimation

JEFF CANDY, *AES Member*

Pietra, San Diego, CA 92126

CLAUS FUTTRUP, *AES Member*

SEAS Fabrikker AS, Norway

We present a methodology to measure transducers with a *dual-added-mass* technique in order to extract the motional impedance $Z_{\mathrm{M}}(\omega)$ and force factor $B\ell$ from the total impedance. This methodology is suitable for determining moving mass and compliance for motional impedance models that include viscoelasticity and frequency-dependent damping by curve fitting, and is applicable to classical transducers for which adding mass to the moving parts is possible without introducing significant artefacts. Furthermore, we discuss techniques to assess the quality of the results. Finally, the quality of the proposed measurement technique is verified with an ANOVA Gage R&R measurement system analysis.

0 INTRODUCTION

A traditional, straightforward technique to estimate loudspeaker parameters is the well-known *added-mass* approach. That is, by adding a known mass to the cone, and comparing the impedance to the unweighted impedance, sufficient information is obtained to determine the required electromechanical parameters. In recent decades, alternative approaches utilizing a laser have been applied: either Doppler-laser which identifies the velocity [1], or a triangulation laser which identifies the position of the loudspeaker cone [2]. The added-mass approach is still used when a laser is not available, e.g. for hobbyist speaker builders. In this paper we propose an approach, which uses two known added masses, and exclusively electrical impedance measurements, to extract the motional impedance. This new approach has the potential to identify the motor strength, $B\ell$, and moving mass, M_{MS}, with higher accuracy than the classical added-mass method. Furthermore, the motional impedance can be analytically isolated, making the new method particularly well-suited for curve fitting to a lumped parameter model for identification of viscoelastic properties. If sufficient care is taken, the method has the potential to offer many of the accuracy benefits of a laser without the cost, or to at least provide an alternative method to compute a high-precision fit to electromechanical parameters.

The new technique we present was motivated by the emergence of modern lumped parameters models that provide some description of the viscoelastic properties of the loudspeaker suspension. Looking back on the history of moving-coil transducers, we see that Olson had already described the traditional model of the mechanical side of a loudspeaker in terms of mass, resistance, and compliance in his 1940 text *Elements of Acoustical Engineering* [3]. Much later, in 1978, Brian Elliott presented an AES paper expressing a realization that the loudspeaker suspension is made from elastomers and shows signs of viscoelastic hysteresis [4]. In this work he appears to coin the expression *frequency-dependent damping*. The observation of frequency dependent damping in the audio frequency range is directly related to the presence of viscoelasticity. Another 15 years later, in 1993, Knudsen and Jensen presented their development of the LOG-model [5] which quantified the viscoelastic *creep effect*. A variation of the LOG model was adopted by Wolfgang Klippel (around 2001) and has since been a kind of de facto industry standard. In recent years a number of newer models have appeared. Although a discussion and comparison of these newer models is beyond the scope of the present work, we remark that they provided the motivation for the present analysis. To this end, the new dual-added-mass method forms the basis for a comprehensive impedance-fitting protocol sophisticated enough to be applicable to these new lumped parameter models.

1 A DUAL-ADDED-MASS TECHNIQUE

1.1 Model-free extraction of motional impedance

The measurement of total (electrical) impedance of an electro-dynamic transducer consists of the *blocked electrical* plus *mechano-acoustic* contributions

$$Z(\omega) = Z_{\mathrm{E}} + Z_{\mathrm{M}} = Z_{\mathrm{E}} + \frac{1}{i\omega C_{\mathrm{MES}} + g(\omega)} \ . \tag{1}$$

In this expression, $\omega = 2\pi f$ is the *angular frequency* of oscillation and f is the frequency in Hz. In the classical Thiele/Small approach, $g(\omega)$ contains the stiffness $L_{\mathrm{CES}} \doteq C_{\mathrm{MS}}(B\ell)^2$ and damping $R_{\mathrm{ES}} \doteq (B\ell)^2/R_{\mathrm{MS}}$, but in a general formulation this part may also include viscoelasticity. As such $g(\omega)$ is a model-independent representation of the stiffness and damping. The only condition which must be met in this formulation is that the moving mass M_{MS}, here represented by the electrical equivalent $C_{\mathrm{MES}} \doteq M_{\mathrm{MS}}/(B\ell)^2$, is fully captured by C_{MES} and does not contribute to g. This implies that radiation impedance (air load) is assumed to be constant in the frequency range of interest (see Appendix A.1).

In the dual-added-mass approach, three measurements of driver impedance are conducted:

1. $Z^{(0)}$ Cone unweighted
2. $Z^{(1)}$ Cone with added mass m_1 attached
3. $Z^{(2)}$ Cone with added mass m_2 attached

The three measurements are then decomposed according to

$$Z^{(0)} = Z_{\mathrm{M}}^{(0)} + Z_{\mathrm{E}} \ , \tag{2}$$

$$Z^{(1)} = Z_{\mathrm{M}}^{(1)} + Z_{\mathrm{E}} \ , \tag{3}$$

$$Z^{(2)} = Z_{\mathrm{M}}^{(2)} + Z_{\mathrm{E}} \ , \tag{4}$$

where Z_{E} is invariant, and

$$Z_{\mathrm{M}}^{(k)} = \frac{1}{i\omega C_k + g(\omega)} \ . \tag{5}$$

Instead of three independent C_k-values, we now take advantage of the fact that we are adding known masses:

$$C_0 = C \ , \tag{6}$$

$$C_1 = C + \Delta C_1 \ , \tag{7}$$

$$C_2 = C + \Delta C_2 \ . \tag{8}$$

In terms of added masses, these are:

$$\Delta C_1 = \frac{m_1}{(B\ell)^2} \quad \text{and} \quad \Delta C_2 = \frac{m_2}{(B\ell)^2} \tag{9}$$

With this in mind, it is possible to extract the pure motional impedance. First the electrical impedance, Z_{E}, which is unchanged during the added-mass operations, is removed from the data by calculating the following differences

$$\begin{aligned} \Delta Z_1 &\doteq Z^{(0)} - Z^{(1)} \\ &= Z_{\mathrm{M}}^{(0)} - Z_{\mathrm{M}}^{(1)} = \frac{i\omega\Delta C_1}{(i\omega C + g)(i\omega C_1 + g)} \ , \end{aligned} \tag{10}$$

$$\begin{aligned} \Delta Z_2 &\doteq Z^{(0)} - Z^{(2)} \\ &= Z_{\mathrm{M}}^{(0)} - Z_{\mathrm{M}}^{(2)} = \frac{i\omega\Delta C_2}{(i\omega C + g)(i\omega C_2 + g)} \ . \end{aligned} \tag{11}$$

In principle, each ΔZ contains no component of electrical impedance, Z_{E}, because it is unchanged between measurements. Therefore each ΔZ contains contributions only from motional impedance. These formulae depend only on measurement data and are independent of fitting to a given compliance model. In terms of the unweighted motional impedance $Z_{\mathrm{M}}^{(0)}$ (which we write as Z_{M} for brevity) we have

$$\Delta Z_1 = \frac{i\omega\Delta C_1 Z_{\mathrm{M}}^2}{1 + i\omega\Delta C_1 Z_{\mathrm{M}}} \ , \tag{12}$$

$$\Delta Z_2 = \frac{i\omega\Delta C_2 Z_{\mathrm{M}}^2}{1 + i\omega\Delta C_2 Z_{\mathrm{M}}} \ . \tag{13}$$

These can be solved for ΔC_1 and ΔC_2, respectively, to yield:

$$i\omega\Delta C_1 = \frac{\Delta Z_1}{Z_{\mathrm{M}}^2 - Z_{\mathrm{M}}\Delta Z_1} \ , \tag{14}$$

$$i\omega\Delta C_2 = \frac{\Delta Z_2}{Z_{\mathrm{M}}^2 - Z_{\mathrm{M}}\Delta Z_2} \ . \tag{15}$$

For the dual-added-mass method to be valid, ΔC_1 and ΔC_2 as defined in Eq. (9) must be independent of frequency. If this condition is satisfied, we can derive an expression for the model-free motional impedance:

$$\frac{\Delta C_2}{\Delta C_1} = \frac{\Delta Z_2}{\Delta Z_1}\frac{Z_{\mathrm{M}} - \Delta Z_1}{Z_{\mathrm{M}} - \Delta Z_2} = \mu \ , \tag{16}$$

where $\mu = m_2/m_1$. Thus, we arrive at the key result; namely, the *model-free motional impedance*:

$$Z_{\mathrm{M}*} = \frac{(1-\mu)\Delta Z_1 \Delta Z_2}{\Delta Z_2 - \mu\Delta Z_1} \ . \tag{17}$$

For clarity, we refer to this *estimate* of the motional impedance as $Z_{\mathrm{M}*}$. Although $Z_{\mathrm{M}*}$ is formally a good approximation to the true Z_{M} as long as ΔC_1 is independent of ω, in practice the accuracy of $Z_{\mathrm{M}*}$ is limited to the region where ΔZ_1 and ΔZ_2 are not too small. A sample calculation is in given Fig. 4 and shows that, in reality, $Z_{\mathrm{M}*}$ is accurate and should be used only in the vicinity of $\omega = \omega_{\mathrm{s}}$, where ω_{s} is the driver resonant frequency. Despite this caveat, there are two evident advantages to the dual-added-mass approach. First, it operates entirely on measurement data without any model assumptions about stiffness or damping. Second, the mechanical impedance is completely isolated, with Z_{E} removed from the problem. In addition to Z_{E}, the amplifier's output impedance (i.e., the generator impedance R_g), the cable impedance, and the series (current sensor) resistor of the measurement equipment are removed from the problem. Note that with this result, we can estimate the resonant frequency of the mechanical system as

$$\omega_{\mathrm{s}} = \underset{\omega}{\mathrm{argmax}}\,(|Z_{\mathrm{M}*}|) = 2\pi f_{\mathrm{s}} \ . \tag{18}$$

In this work, a precise determination of the resonant frequency based purely on data is not necessary insofar as it will be derivable from motional fit parameters to be determined in the sections that follow. We also remark that

the resonant frequency as defined in Eq.(18) does not exactly coincide with the location of $\mathrm{Im}\, Z_{\mathrm{M}*} = 0$ due to the frequency-dependence of the effective damping (i.e., the real part of g). Thus there is potential ambiguity with respect to the definition of ω_s in viscoelastic systems.

To provide a noticeable shift in the resonant frequency and thereby detect the viscoelastic properties with sufficient precision, we generally recommend that m_2 is close to the transducer's moving mass, and that m_1 is approximately half the moving mass. These choices will produce shifts of about 40% and 20%, respectively, in the resonant frequency ω_s.

1.2 Estimation of $B\ell$

Based on Eqs. (9) and (14), $B\ell$ is calculated as

$$(B\ell)^2 = \frac{m_1}{\Delta C_1} = m_1 \,\mathrm{Re}\left\langle \frac{i\omega Z_{\mathrm{M}*}(Z_{\mathrm{M}*} - \Delta Z_1)}{\Delta Z_1} \right\rangle_{\omega_1}^{\omega_2} , \quad (19)$$

where the angle brackets denote an average. For each measurement point in frequency, a $B\ell$ value can be extracted and hence it is possible to plot a $B\ell(\omega)$ curve. An example of this curve is shown in Fig. 5. Of course, $B\ell$ in the model does not change with frequency, so it remains to select a suitable frequency range for the average in Eq. (19). We recommend $\omega_1 = 0.8\omega_s$ and $\omega_2 = 1.2\omega_s$, where ω_s is determined by Eq. 18. For the average to be meaningful, a flat area of the $B\ell(\omega)$ curve must be found. Typically, provided the measurements are good, this occurs in the vicinity of the free-air resonant frequency of the driver. In this was, $B\ell$ may be determined *without* any model assumptions about $g(\omega)$.

The accurate determination of $B\ell$ is crucial for success with the added-mass method, and ensures we can reliably transform parameters from the mechanical to the electrical domain.

1.3 Estimation of M_{MS}

In this section we will describe a method to deduce the moving mass M_{MS}, along with other motional fit parameters, from motional data $(Z_{\mathrm{M}*})_j$. For this we need to choose a specific lumped-parameter model. In what follows, all fitting results will be based on the LOG compliance model [5] for the motional impedance

$$g(\omega) \doteq \frac{1}{R_0} + \frac{\sigma(\omega)}{i\omega L_0} , \quad (20)$$

where σ is a complex factor that describes viscoelastic creep and frequency-dependent damping

$$\sigma = \frac{1}{1 - \beta \ln(i\omega)} . \quad (21)$$

Note that the traditional Thiele-Small form is obtained by setting $\beta = 0$ so that $\sigma = 1$. If, for a moment, we consider that the value of β is known, then we can write a linear equation for the motional parameters,

$$\frac{1}{Z_{\mathrm{M}*}} = i\omega\, a + b + \frac{i\sigma(\omega)}{\omega} c , \quad (22)$$

where for brevity we have defined $a = C_{\mathrm{MES}}$, $b = 1/R_0$ and $c = -1/L_0$. This simple form implies that we can obtain a coefficient solution by linear least squares. To do this, we define the error functional (the squared norm of the residual)

$$\varepsilon_\beta(a,b,c) \doteq \sum_j \left[\left(b - \frac{\sigma_I(\omega)}{\omega_j} c - \mathrm{Re}\, Y_j \right)^2 \quad (23)$$

$$+ \left(\omega_j a + \frac{\sigma_R(\omega_j)}{\omega_j} c - \mathrm{Im}\, Y_j \right)^2 \right] , \quad (24)$$

where

$$Y_j \doteq \frac{1}{(Z_{\mathrm{M}*})_j} \quad (25)$$

is the motional admittance. Here, $\sigma_R = \mathrm{Re}\,\sigma$ and $\sigma_I = \mathrm{Im}\,\sigma$. The summation variable j denotes a suitable subdomain of the frequency range. For the analysis in the present paper, we choose values of j for which $0.8\omega_\mathrm{s} < \omega_j < 1.2\omega_\mathrm{s}$. Taking the partial derivatives of ε with respect to a, b and c yields the following linear equations for the minimum norm of the residual:

$$\begin{bmatrix} \sum_j \omega_j^2 & 0 & \sum_j \sigma_R(\omega_j) \\ 0 & \sum_j 1 & -\sum_j \frac{\sigma_I(\omega_j)}{\omega_j} \\ \sum_j \sigma_R(\omega_j) & -\sum_j \frac{\sigma_I(\omega_j)}{\omega_j} & \sum_j \frac{\sigma_R^2 + \sigma_I^2}{\omega_j^2} \end{bmatrix} \begin{bmatrix} a_0 \\ b_0 \\ c_0 \end{bmatrix}$$

$$= \begin{bmatrix} \sum_j \omega_j \,\mathrm{Im}\, Y_j \\ \sum_j \mathrm{Re}\, Y_j \\ \sum_j \frac{\sigma_R \,\mathrm{Im}\, Y_j - \sigma_I \,\mathrm{Re}\, Y_j}{\omega_j} \end{bmatrix} \quad (26)$$

More precisely, $\varepsilon_\beta\,[a_0(\beta), b_0(\beta), c_0(\beta)]$ represents the minimum residual at fixed β. A further 1-dimensional minimization of ε_β over β is required to find the true minimum. Let us denote the result of this final minimization as β_0, which can be obtained using any standard 1D minimization scheme. Then, the moving mass is given by $M_{\mathrm{MS}} = (B\ell)^2 a_0(\beta_0)$. This fitting process also determines the effective resistance R_0 and compliance L_0, as well as the creep parameter β.

To be clear, we repeat that for a given β, the inputs to Eq. (26) are Y_j and the frequencies ω_j, whereas the outputs are C_{MES}, R_0 and L_0. We use β for viscoelasticity expressed using a natural logarithm, but this may be easily converted to classical λ values utilizing the base-10 LOG representation as detailed in Appendix A.4.

1.4 Equivalent R_{ES} and L_{CES}

It is of some interest to determine equivalent values for R_{ES} and L_{CES} in the LOG model that can be compared with

traditional Thiele-Small parameters. Although the correspondence is not unique, a simple method approach is to set

$$g(\omega_s) \doteq \frac{1}{R_{ES}} + \frac{1}{i\omega_s L_{CES}} \ . \tag{27}$$

Then, some algebra shows that

$$\frac{1}{L_{CES}} = \frac{1}{L_0} \frac{1 - \beta \ln(\omega_s)}{(1 - \beta \ln \omega_s)^2 + (\pi\beta/2)^2} \ , \tag{28}$$

$$\frac{1}{R_{ES}} = \frac{1}{R_0} + \frac{1}{\omega_s L_0} \frac{\pi\beta/2}{(1 - \beta \ln \omega_s)^2 + (\pi\beta/2)^2} \ . \tag{29}$$

1.5 Mass consistency check

We propose a type of consistency check that can provide a critical assessment of the data quality. First, using the model-free impedance Z_{M*}, we can check for mass consistency using

$$m_1^* = \mathrm{Re}\left[\frac{(B\ell)^2}{i\omega} \frac{\Delta Z_1}{Z_{M*}(Z_{M*} - \Delta Z_1)} \right] \ . \tag{30}$$

The right-hand side will be independent of ω if Eq. (1) is valid. Also, since we have fitted Z_M to a specific model to determine M_{MS}, it is possible to utilize this fit to calculate mass consistency for the added masses m_1 and m_2:

$$m_1^{\mathrm{fit}} = \mathrm{Re}\left[\frac{(B\ell)^2}{i\omega} \frac{\Delta Z_1}{Z_M^{\mathrm{fit}}(Z_M^{\mathrm{fit}} - \Delta Z_1)} \right] \ , \tag{31}$$

$$m_2^{\mathrm{fit}} = \mathrm{Re}\left[\frac{(B\ell)^2}{i\omega} \frac{\Delta Z_2}{Z_M^{\mathrm{fit}}(Z_M^{\mathrm{fit}} - \Delta Z_2)} \right] \ . \tag{32}$$

The right-hand sides will be independent of ω if $g(\omega)$ is a good model of the stiffness and damping. The results may be compared (e.g. plotted) relative to the nominal masses; that is, can plot m_1^{fit}/m_1 and m_2^{fit}/m_2 and comparee with m_1^*/m_1 to assess a frequency range around ω_s where the data is good. An example of this mass consistency check is shown in Fig. 8.

2 EXAMPLE TRANSDUCER ANALYSIS

To illustrate the complete procedure for determination of the motor strength $B\ell$ and moving mass M_{MS}, we carry out the analysis for a SEAS L16RNX (H1488-08) mid-woofer. This driver, shown in Fig. 1, has an aluminium cone and dust cap, making it a robust choice for repeated added-mass measurements. Moreover, the motional parameters are broadly representative of mid-size transducers. All free-air measurement data is collected with the driver mounted into a stand, which can be purchased with the Klippel Distortion Analyzer equipment, to secure it firmly in place. According to preliminary linear parameter measurements (LPM) on a Klippel DA1 system, the L16RNX has $M_{MS} \simeq 15.3\,g$ and $B\ell \simeq 7.14\,\mathrm{Tm}$.

Fig. 1. SEAS L16RNX (H1488-08) mid-woofer mounted in stand.

The equipment used for collection of impedance data is a Smith & Larson Woofer Tester Pro (WTPro), which employs a $0.5\,\Omega$ reference resistor in combination with an external amplifier to measure impedance at desirable voltage/power levels. Here, a Benchmark AHB2 amplifier is used, which has excellent signal-to-noise ratio and bandwidth, low output impedance, and is suitable for laboratory use (with advanced overload protection). The WTPro is calibrated and the calibration saved to a PC. This calibration was performed once at the beginning of the test period which ran from 30 November 2016 until 11 February 2017.

Fig. 2. SEAS L16RNX (H1488-08) mid-woofer mounted in stand with added mass m_1.

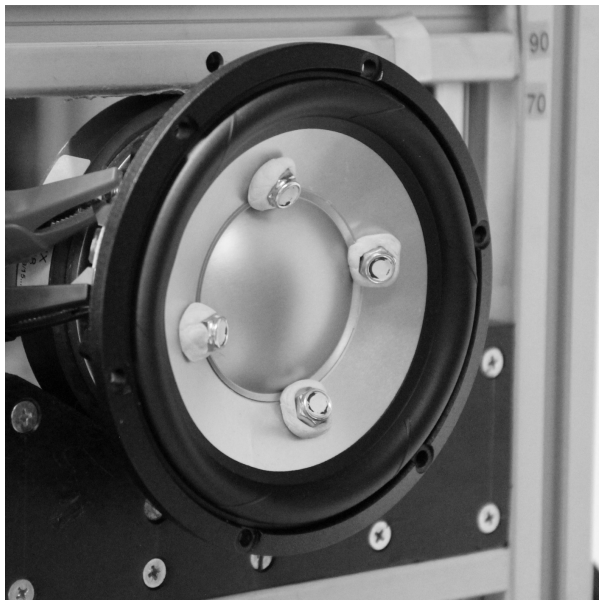

Fig. 3. SEAS L16RNX (H1488-08) mid-woofer mounted in stand with added mass m_2.

The setup used in the WTPro is a steady-state sine wave signal, which is stepped 384 times in the frequency range $10\,\text{Hz} \leq f \leq 20\,\text{kHz}$, giving a sufficiently high resolution (about 35 points per octave) even for weakly-damped drivers. The output was chosen to be approximately 242 mV (the WTPro monitors and shows the Voltage range of 237 mV to 247 mV within the measured frequency range). Our understanding is that this small variation in voltage is corrected for and thus does not affect the accuracy of $Z(\omega)$. Note that, into a $6\,\Omega$ load, this voltage setting is equivalent to approximately 10 mW. Choosing a suitable drive level for the measurements is typically a trade-off between good signal-to-noise ratio (which favors high voltage) and low nonlinearity (which favors low voltage). By selecting 242 mV, we achieve a good trade-off between the two and the data appears to be both low-noise [1] and free of significant nonlinear effects. Although the dual-added-mass method could be used for scanning at higher power levels, such an analysis is beyond the scope of the present paper.

2.1 Calculation of $Z_{\text{M}*}$

The added masses were kept in line with the Klippel estimate of M_{MS} by choosing $m_2 \simeq 16.048\,\text{g}$ and $m_1 \simeq 8.017\,\text{g}$. These were carefully measured *a posteriori* on a precision scale with 1 mg resolution. These choices are consistent with our guidelines of $m_2 \simeq M_{\text{MS}}$ and $m_1 \simeq M_{\text{MS}}/2$. The masses are mounted in 4 pieces (representing m_2, as shown in Fig. 3) so that diagonally one can remove a pair and then remeasure with 2 pieces (representing m_1, as shown in Fig. 2). This procedure keeps the overall moving mass in balance to prevent rocking modes. The masses are further kept within about 1% of each other, and the location of each mass on the cone registered individually. The masses are attached onto the cone near the dust cap for close proximity to the voice coil and to minimize the dynamic load on the cone (i.e., to minimize bending). The care one must take in doing added-mass measurements is well known in the industry and certainly applies for the present dual-added-mass method. In particular, it is important to avoid moving the cone excessively so that the viscoelastic suspension is not stretched between the three impedance measurements. Doing so would adversely affect the compliance, especially at low frequency, due to the memory effect. This is most important for drivers with a highly viscoelastic suspension (such as the Vifa P17WJ00-08) and less important for those with less viscoelastic suspension (like the present L16RNX).

Measurements with 385 data points were resampled with spline interpolation so that a total of 1200 data points were available for processing and to ensure all plotted curves are smooth. The method for resampling is described briefly in Appendix A.2. Thus, we measure $Z^{(2)}$ (with m_2), then $Z^{(1)}$ (with m_1), and finally the unweighted driver to obtain $Z^{(0)}$. With these measurements, we compute ΔZ_1 and ΔZ_2. Then, using Eq. (17), we compute the model-free estimate $Z_{\text{M}*}$ for the motional impedance. The three measurements together with the calculated $Z_{\text{M}*}$ are illustrated in Fig. 4. From Eq. (18), we find $f_{\text{s}} = 45.5\,\text{Hz}$.

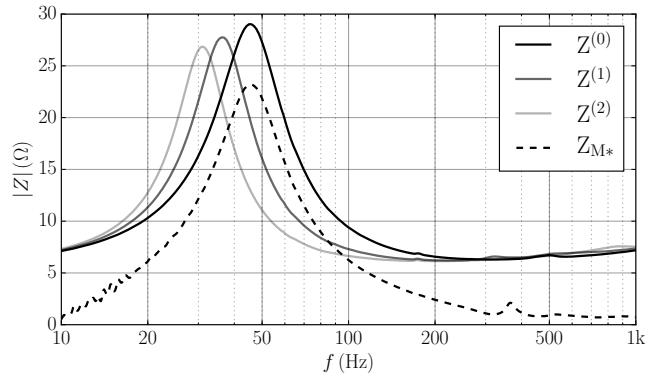

Fig. 4. Impedance measurements $Z^{(0)}$, $Z^{(1)}$, and $Z^{(2)}$, and the derived motional impedance $Z_{\text{M}*}$. Only the magnitudes are plotted. Notice that Z_{M} is formulated such that it corresponds to the free-air measurement, $Z^{(0)}$.

2.2 Calculation of $B\ell$

Next, with the computed data for $Z_{\text{M}*}$, we use Eq. (19) to estimate $B\ell$. For the purpose of averaging, we set $\omega_1 = 0.8\,\omega_{\text{s}}$ and $\omega_2 = 1.2\,\omega_{\text{s}}$, where $\omega_{\text{s}} = 2\pi f_s$. The computed average, $B\ell \simeq 7.007$, is illustrated with a horizontal black line in Fig. 5 superimposed on the frequency-dependent function $B\ell(\omega)$. The shaded area indicates the averaging region. A more detailed view of the same data is given in Fig. 6.

[1] We have verified that the tester is capable of maintaining a good S/N below 100 mV

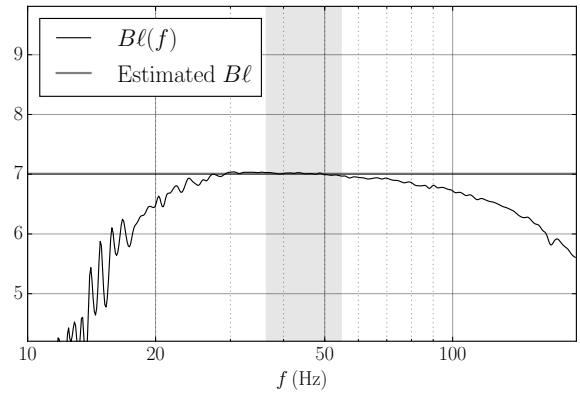

Fig. 5. Estimate of $B\ell$ via average over fitting range (shaded) $0.8f_s \leq f \leq 1.2f_s$, where $f_s = 45.5$ Hz. The horizontal black line denotes the average value $B\ell = 7.007$.

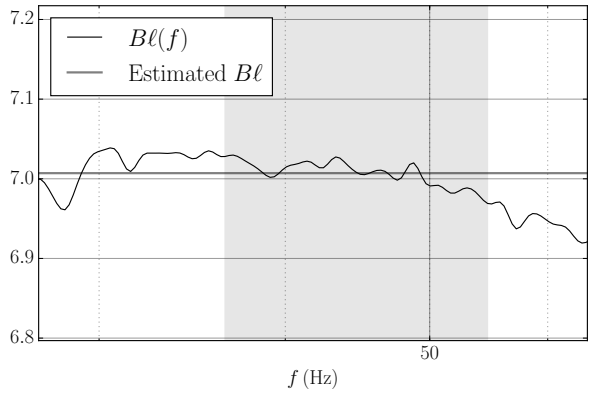

Fig. 6. Zoomed-in view of previous figure. As before, the shaded area indicates the averaging window used to compute $B\ell$.

2.3 Calculation of M_{MS}

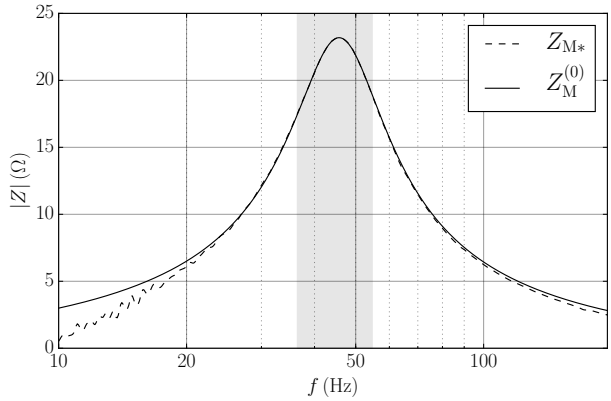

Fig. 7. Comparison of $Z_{\mathrm{M}*}$ with fit function $Z_{\mathrm{M}}^{(0)}$. Fit parameters were computed using the least-squares minimization of Eq. (26) over the shaded region.

Solving the linear system in Eq. (26), based on the Knudsen LOG model as defined in Eqs. (20) and (21), we find $M_{\mathrm{MS}} \simeq 15.05$ g. The solution of the system of linear equations also yields $\beta \simeq 0.059$ with $R_0 \simeq 32.20\,\Omega$ and $L_0 \simeq 60.24$ mH. According to the conversion formula, these (approximately) correspond to traditional Thiele-Small values of $R_{\mathrm{ES}} \simeq 23.2\,\Omega$ and $L_{\mathrm{CES}} \simeq 40.8$ mH. A comparison between the fit Z_{M} and the original model-free function $Z_{\mathrm{M}*}$ is shown in Fig. 7. The fit is exceptional in the shaded fit region. Outside the fit region, it may appear as though the fit is poor, but a more reasonable interpretation is that the quality of $Z_{\mathrm{M}*}$ – as we have emphasized repeatedly – diminishes rapidly away from the vicinity of resonance.

2.4 Mass consistency

We can examine the quality of the present results using the mass-consistency test described in Sec. 1.5. Figure 8 show a calculation of the model-free mass ratio m_1^*/m_1 as well as the model-dependent mass ratios. The latter are computed using $Z_{\mathrm{M}}^{\mathrm{fit}}$ as fit to the LOG model. In all cases we get a broad range of consistency in the vicinity of f_s. As we have remarked previously, the validity of $Z_{\mathrm{M}*}$ is limited to a narrow frequency range around f_s, and this corroborated by Figure 8. The plot is also strong evidence for the LOG model fit to Z_{M} being more accurate than $Z_{\mathrm{M}*}$ far from resonance. More specifically, the fit consistency is very good over a wide region (up to at least 100 Hz). On the other hand, below f_s, the mass consistency is not quite so good. We speculate that this is caused by the term $i\omega C_k$ in Eq. (5) becoming progressively smaller in the low-frequency range and thus more sensitive to errors in compliance.

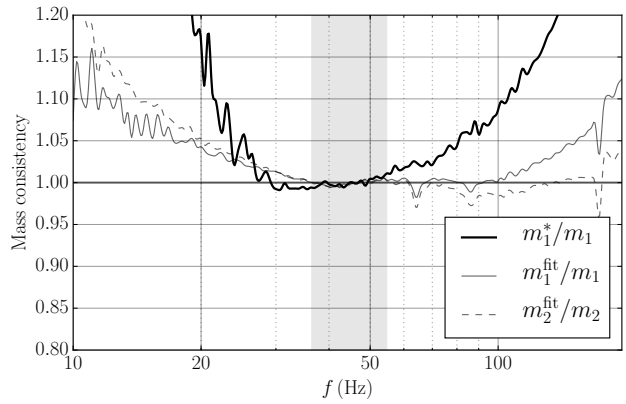

Fig. 8. Mass consistency.

3 MEASUREMENT SYSTEM ANALYSIS

A classical method to evaluate the quality of a measurement procedure, such as the dual-added-mass method suggested in this paper, is to conduct a measurement system analysis (MSA). Typically, this is in the form of a Gage R&R statistical analysis (for example ANOVA) to evaluate the precision (not accuracy) of the measurement procedure. First, sources of variation must be identified (e.g., SWIPE):

- Standard
- Workpiece (Part variation)
- Instrument (Gage)
- Person/Procedure (Appraiser)
- Environment

Standard could be equipment calibration, or compatibility between device under test (DUT) and instrument, and so on. We don't track or evaluate this. *Workpiece* requires that we measure more than one driver. We don't track this. *Instrument* and *appraiser* are what we can track here, since we have 4 appraisers and a total of 20 measurements. Finally, *Environment*, which could include atmospheric variation, or vibration, or quality of the measurement stand, is not tracked. For details, see page 17 of Ref. [6].

In the present MSA, we decided to not strictly follow standard procedures and instead measure only one driver (i.e., one part). This decision reflects our interest in the quality of the suggested method in regard to repeatability and reproducibility, rather than in component variation (as in production setups). The chosen H1488-08 (L16RNX) driver is both robust and handy. By robust, we mean that one can apply m_1 and m_2 repeatedly without significant damage to the driver. In fact, during testing, the aluminum cone was dented slightly without affecting measurements. In contrast, Blu-Tack applied to a paper-cone woofer can more easily damage the cone by tearing the fibers. Also, the suspension is such that C_{MS} changed only slightly during the measurement procedure. By handy, we simply mean the driver is small and light enough to easily mount and unmount from the measurement rack. For this reason, the L16 may represent a *best case* scenario when it comes to stability in the MSA. We believe this is the appropriate first step. Performing a worst-case scenario MSA, although it may illustrate the robustness of the measurement procedure, is more challenging as the analysis becomes dominated by quirks and challenging features of the driver. We also remark that the driver suspension properties may change over time as reapplying the masses stretches the suspension and thereby changes C_{MS}. However, this does not influence our estimation of $B\ell$ and M_{MS}.

Four people were asked to perform five measurements each, so that the driver was measured 21 times in total. For the most part, one or occasionally two measurements were performed each day, and the equipment was turned off and disconnected between each measurement. The added masses were remeasured following each measurement. Sometimes, but not always, they would be refreshed with new Blu-Tack. Because the masses are measured each time, the statistical analysis reflects the true statistical variation. A single, complete measurement (that includes three impedance sweeps with mass recording) takes about 40-60 minutes. Those who wish to employ the presented dual-added-mass technique are encouraged to perform a Gage R&R analysis with their own equipment to verify the measurement setup. This section presents the results as performed at SEAS Fabrikker AS in Norway using available in-house equipment.

3.1 MSA Results

A list of all 21 measurements is shown in Table 1, including date of measurement, added-mass values, and computed $B\ell$ and M_{MS}.

ID	Date Y-M-D	m_1 (g)	m_2 (g)	$B\ell$ (Tm)	M_{MS} (g)
A	16-11-30	8.017	16.048	7.007	15.05
A	17-01-20	8.910	17.865	7.065	15.18
B	17-01-26	8.909	17.868	7.047	15.18
B	17-01-30	8.904	17.865	6.999	15.00
B	17-02-01	8.960	17.862	6.999	14.97
C	17-02-01	8.419	17.862	6.679	13.06
A	17-02-01	9.028	18.028	7.025	15.11
A	17-02-02	9.032	18.032	6.998	14.97
B	17-02-02	9.029	18.028	7.075	15.22
B	17-02-03	9.032	18.033	6.878	14.46
D	17-02-03	9.030	18.029	7.035	14.94
C	17-02-03	8.999	18.032	7.037	15.11
C	17-02-04	9.011	17.999	7.071	15.23
D	17-02-06	8.986	17.982	6.928	14.53
C	17-02-06	8.998	17.998	7.031	15.13
D	17-02-07	9.011	18.018	7.069	15.29
C	17-02-07	8.992	17.991	7.032	15.17
D	17-02-08	9.006	18.018	7.020	15.20
C	17-02-08	8.993	17.997	7.047	15.26
A	17-02-10	8.990	17.999	7.025	15.21
A	17-02-11	8.992	18.000	7.026	15.19

Table 1. Overview of measurements for the MSA, sorted by date and time. Here, A-D refer to the four different individuals who carried out independent driver testing, with m_1 and m_2 the added-mass values applied by the tester. Above, $B\ell$ is the model-independent value of the force factor inferred from the data, and M_{MS} is the moving mass computed by fitting $Z_{\mathrm{M}*}$ to the LOG compliance model. The measurements marked with grey background were erroneous and discarded from further analysis.

Based on a series of diagnostics, three measurements were identified as flawed and subsequently rejected. The reasons for each rejection are outlined in more detail in Appendix A.3. Regarding the dates for each operator's trial, we remark that the measurements are not performed in a streamlined way but in a somewhat random manner which is the recommended procedure for Gage R&R. Figure 9 shows the correlation between $B\ell$ and M_{MS} for the remaining 18 measurements in the MSA. In Fig. 9, we can see that the measurements are bounded by $6.99\,\mathrm{Tm} < B\ell < 7.08\,\mathrm{Tm}$ and $14.9\,\mathrm{g} < M_{\mathrm{MS}} < 15.3\,\mathrm{g}$. This leads us to conclude the proposed measurement technique is capable of detecting $B\ell$ precisely with a tolerance of about $\pm 0.5\%$, and M_{MS} with a tolerance of about $\pm 1\%$. Because M_{MS} is computed using the formula $M_{\mathrm{MS}} = (B\ell)^2 C_{\mathrm{MES}}$, this produces a correlation between errors; that is, the errors $\delta B\ell$ and δC_{MES} will propagate to δM_{MS} according to

$$\frac{\delta M_{\mathrm{MS}}}{M_{\mathrm{MS}}} \sim 2\,\frac{\delta B\ell}{B\ell} + \frac{\delta C_{\mathrm{MES}}}{C_{\mathrm{MES}}}\,. \tag{33}$$

And indeed, the trendline in Fig. 9 gives a slope of 1.45 which is close to the theoretical value of 2 in Eq. 33. In fact, plotting the trendline for C_{MES} versus $B\ell$ in Fig. 10 shows a much weaker, negative correlation. Substituting $\delta C_{\mathrm{MES}}/C_{\mathrm{MES}} = -0.55\,\delta B\ell/B\ell$ into Eq. (33) is consistent with the correlation (slope 1.45) seen in Fig. 9. For this

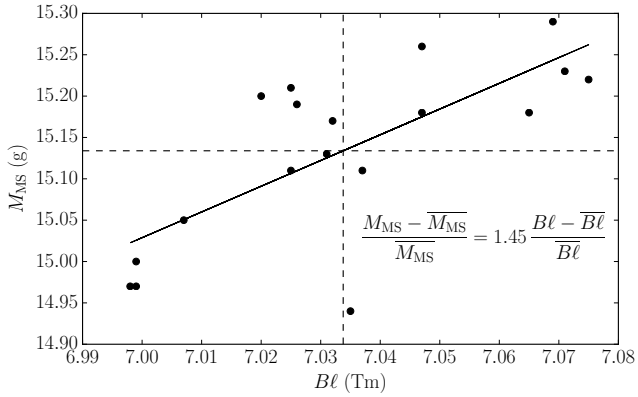

Fig. 9. Raw $(B\ell, M_{\mathrm{MS}})$ data plotted against linear trend-line showing significant correlation. When C_{MES} is plotted as a function of $B\ell$ there is no evident correlation. The mean values here are $\overline{B\ell} = 7.034\,\mathrm{Tm}$ and $\overline{M_{\mathrm{MS}}} = 15.13\,\mathrm{g}$.

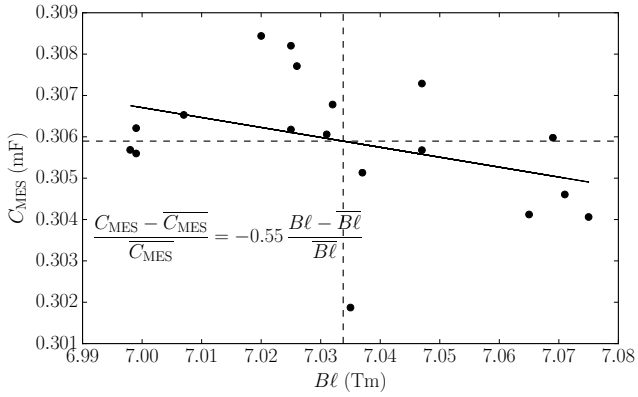

Fig. 10. Raw $(B\ell, C_{\mathrm{MES}})$ data plotted against linear trend-line showing weaker correlation. The mean values here are $\overline{B\ell} = 7.034\,\mathrm{Tm}$ and $\overline{C_{\mathrm{MES}}} = 0.306\,\mathrm{mF}$.

reason, we conclude that any error in $B\ell$ is amplified in the calculation of M_{MS}.

In this MSA we decide to study the statistical distribution of $B\ell$ since this is the key parameter for the measurement procedure. To this end, it is illustrative to reexamine the data series with measurement index sorted by data (see Fig. 11) and by appraiser (see Fig. 12). To study the accuracy of the method and how well it complies with a normal distribution, a bias study is performed. A plot of the $B\ell$ dataset histogram is shown in Fig. 13. The tentative conclusion is that the distribution is non-normal, but nevertheless we will proceed with the statistical analysis.

3.2 ANOVA Gage R&R

Having outlined the data collection method and provided a justification for rejection of outliers, we are now in a position to continue with a formal ANOVA Gage R&R treatment. Here, ANOVA means *Analysis of Variance* and is a more sophisticated technique than the so-called *Average and Range* method. The ANOVA – or more specifically, the one-way ANOVA – requires more calculation but estimates the variances and their interactions in a statistically sound manner. First we define the sum of squared differences (SS) for the *appraiser* (A), the *equipment* (E), and the *total* (T):

$$\mathrm{SS}_A \doteq \sum_{k=1}^{N_A} r_k (\bar{x}_k - \bar{x})^2 \ , \tag{34}$$

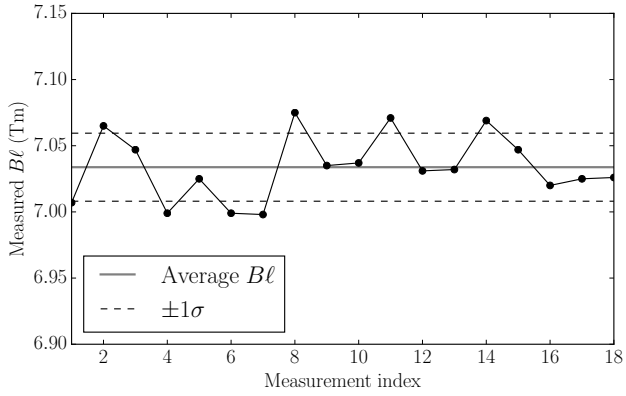

Fig. 11. $B\ell$ as a function of measurement index sorted by date. Average $B\ell$ and 1-σ bounds, as determined by unbiased (total) sample standard deviation.

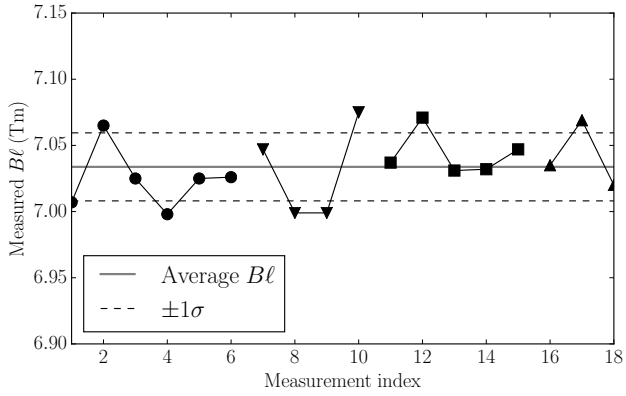

Fig. 12. $B\ell$ as a function of measurement index sorted by appraiser. Average and bounds same as for previous figure.

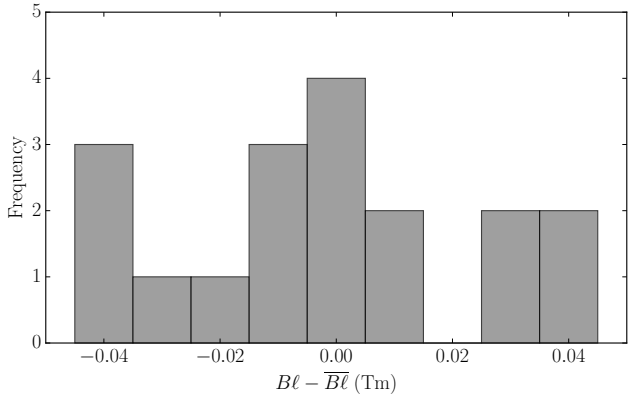

Fig. 13. Bias histogram of the complete 18-point dataset for $B\ell$. This result shows significant deviation from a normal distribution. The results show deviation from the point closest to the mean (index 16 of the previous figure).

$$\mathrm{SS}_E \doteq \sum_{k=1}^{N_A}\sum_{j=1}^{r_k}(x_{jk}-\bar{x}_k)^2 \ , \tag{35}$$

$$\mathrm{SS}_T = \sum_{k=1}^{N_A}\sum_{j=1}^{r_k}(x_{jk}-\bar{x})^2 = \mathrm{SS}_A + \mathrm{SS}_E \ . \tag{36}$$

Above, N_A is the number of appraisers (4 people), r_k is number of repetitions for the k^{th} appraiser, x_{jk} is the j^{th} measurement for appraiser k, $\bar{x}_k$ is the mean for appraiser k, and $\bar{x}$ is the grand mean. Referring to Table 1, we see that

$$\{r_1, r_2, r_3, r_4\} = \{6,4,5,3\} \ , \tag{37}$$

$$N \doteq \sum_{k=1}^{N_A} r_k = 18 \ . \tag{38}$$

We can also define the mean square (MS) values $\mathrm{MS}_x = \mathrm{SS}_x/\mathrm{DF}_x$, where DF refers to the degrees of freedom. Thus,

$$\mathrm{DF}_A = N_A - 1 = 3 \ , \tag{39}$$

$$\mathrm{DF}_E = N - N_A = 14 \ , \tag{40}$$

$$\mathrm{DF}_T = N - 1 = 17 \ . \tag{41}$$

The numerical values of these quantities are summarised in Table 2, below.

Source	**DF**$_x$	**SS**$_x$ (%)	**MS**$_x$ (%)
Appraiser	3	0.1246	0.04153
Equipment	14	0.9247	0.06605
Total	17	1.0493	-

Table 2. ANOVA table summarizing degrees of freedom (DF), sum of squared differences (SS) and mean square (MS) values.

The ANOVA method assumes that there are two separate normal distributions: a single appraiser will sample from a normal distribution with mean $\bar{x}_k$ with deviation σ_E caused by the equipment, whereas the appraiser means are themselves distributed normally with mean $\bar{x}$ and deviation σ_A caused by the differences in appraisals. Based on the above findings, we may calculate *equipment variation* (EV) – a measure of repeatability – using a 3σ (or 99.7%) confidence interval (sometimes, other factors are applied)

$$\mathrm{EV} = 3\sigma_E \sim 3\sqrt{\mathrm{MS}_E} = 0.07710 \ . \tag{42}$$

Normally, the *appraiser variation* $\mathrm{AV} = 3\sigma_A$ – a measure of reproducibility – is estimated to be proportional to $\sqrt{\mathrm{MS}_A - \mathrm{MS}_E}$. Since $\mathrm{MS}_A < \mathrm{MS}_E$, we conclude that AV is insignificant, or at least it cannot be estimated by the ANOVA method. The resulting measurement system R&R is

$$GRR \sim \mathrm{EV} = 0.07710 \ , \tag{43}$$

and we conclude that the variation in the proposed methodology *does not* stem from people and procedure (appraiser) but from the equipment error. Since EV and GRR are related to the standard deviations and have the same units as the measured data ($B\ell$ in Tm), the values are directly comparable. We have a nominal value of $\overline{B\ell} = 7.03\,\mathrm{Tm}$ and a 3σ confidence interval of 0.07, i.e. $\pm 1.0\%$. Hence the method shown here is valid for measuring $B\ell$ with high precision and statistical confidence.

4 CONCLUSION

In this paper we have described a dual-added-mass method to estimate the force factor $B\ell$, the mechanical parameters M_{MS}, C_{MS}, R_{MS} as well as the creep parameter β. The method is more robust and accurate than the usual single-added-mass approach insofar as the blocked electrical impedance can be completely filtered out of the total impedance and the subsequent analysis carried out on the motional impedance only. To quantify the accuracy of the new method, we have carried out an ANOVA MSA analysis using four appraisers, with the result that $B\ell$ can be estimated to $\pm 1\%$ accuracy with a 99% confidence interval using the WTPro measurement system together with sufficiently accurate determination of added masses (added masses were known with $\pm 0.1\%$ accuracy). The results show a $B\ell$ which deviates from Klippel LPM by 1.6% and from the official datasheet by 2.4%.

It seems that the data found by the Klippel LPM measurement is optimistic about $B\ell$ since even the highest $B\ell$ value in our measurement is lower than the Klippel LPM measurement, but please also notice the difference between our average value and the Klippel LPM is less than 2%, so it is not a big disagreement. We emphasize that the present MSA does not clarify the absolute accuracy of the measurements, only the precision between the measurements. To determine the accuracy of a measurement, the equipment must be calibrated with traceability to an accredited laboratory.

5 ACKNOWLEDGEMENTS

Thanks to engineers at SEAS Fabrikker AS for participating in the Gage R&R analysis: Diego Ivars, Håvard Sollien and Peter Brooks. Thanks also to Keith Larson for helpful discussions related to accuracy and constant-voltage testing with the Smith & Larson WTPro.

6 REFERENCES

[1] J. N. Moreno and H. Bøg, "Measurements of Loudspeaker Parameters Using a Laser Velocity Transducer – An Improved Method," in: *Audio. Eng. Soc. Convention 91*, October, 1991.

[2] U. Seidel and W. Klippel, "Fast and Accurate Measurement of the Linear Transducer Parameters," in: *Audio. Eng. Soc. Convention 110*, May, 2001.

[3] H. F. Olson, "Elements of Acoustical Engineering," Van Nostrand, New York, 1940.

[4] B. J. Elliott, "Accurate Methods for Determining the Low-Frequency Parameters of Electro-Mechanical-Acoustic Transducers with BLI Excitation," in: *Audio. Eng. Soc. Convention 61*, November, 1978.

[5] M. H. Knudsen and J. G. Jensen, "Low-Frequency Loudspeaker Models That Include Suspension Creep," *J. Audio. Eng. Soc.*, vol. 41, p. 3, 1993.

[6] M. Down, F. Czubak, G. Gruska, S. Stahley, D. Benham, "Measurement System Analysis, Reference Manual, Fourth Edition," AIAG, 2010.

[7] L. L. Beranek and T. J. Mellow, "Acoustics: Sound Fields and Transducers," Elsevier – Academic Press, Oxford, 2012.

[8] E. S. Olsen and K. Thorborg, "Diaphragm Area and Mass Nonlinearities of Cone Loudspeakers," in: *Audio. Eng. Soc. Convention 99*, October, 1995.

[9] K. Thorborg, C. Tinggaard, F. Agerkvist, C. Futtrup, "Frequency Dependence of Damping and Compliance in Loudspeaker Suspensions," *J. Audio. Eng. Soc.*, vol. 58, p. 472, 2010.

A.1 Variation of effective mass with frequency

Radiation impedance

In addition to the contribution of the suspension components to the motional impedance, the coupling of the diaphragm to the surrounding air results in a non-negligible *radiation impedance*. The precise form of this impedance is a very complicated function of the baffle and cone geometry, and thus no simple formula is available. However, at low frequency, and assuming the motion to be pistonic, the radiation impedance is dominantly reactive and to a good approximation behaves like an effective mass

$$\mathbb{Z}_{\text{rad}} \sim i\omega M_{\text{rad}} \ , \tag{1}$$

For a typical driver measurement setup, the effective mass is minimized if the driver is unbaffled and radiates in a dipolar fashion. In this case, $M_{\text{rad}} = 8a^3\rho/3$ [7], where a is the effective radius of the radiator and ρ is the density of air. On the contrary, the effective mass is maximized if the driver is fully baffled (mounted on a baffle of infinite area), for which $M_{\text{rad}} = 16a^3\rho/3$ [7]. Consider the example of a driver of radius 5.75 cm like the H1488-08 (L16RNX). This corresponds to an unbaffled mass of 0.61 g at $20°C$. Note that the frequency-dependent correction to the low-frequency limit of the effective mass is indeed small; for the 5.75 cm driver, the correction factor for the effective mass (i.e., for the reactive contribution) in an infinite baffle (rather than for the unbaffled case which is more complicated) is

$$\mathbb{Z}_{\text{rad}} \sim i\omega M_{\text{rad}} \left[1 - \frac{4}{15}(ka)^2\right] \ . \tag{2}$$

Here, we can write $\omega = c_s k$ where c_s is the speed of sound, and k is the wavenumber. At 185 Hz, well above the range where the moving mass dominates the impedance, the correction term (in square brackets) amounts to only a 1% reduction in the air load. Because, at low frequencies, the air load is only 4% of the total moving mass, the frequency dependence of $\mathbb{Z}_{\text{rad}}$ changes the moving mass by only 0.04%. Thus, in what follows, we will consider the effect of the radiation impedance to be constant and lumped together with the physical moving mass, M_{MS}, of the diaphragm.

Effective diaphragm area

A large excursion level could influence how much of the suspension is included in the moving mass and thus the effective diaphragm area [8]. For the measurements in this paper, input voltage is kept low in order to minimize the nonlinear effects from excursion.

A.2 Resampling data

Measurement data may occur either linearly-spaced or logarithmically-spaced (log-spaced) in frequency, and the number of datapoints may be different than what is desired for the fitting procedure. In this appendix we present a resampling method which converts arbitrary measurement data into a specified number of with log-spaced data points. This procedure is convenient for modifying measurement data in many different situations (not just the present one). In this paper the resampling algorithm is applied to the raw impedance measurement data, and ensures that there is sufficient resolution around the resonant frequency of a transducer.

Input is in frequency, magnitude, phase (FMP) format, and we wish to resample from n points to N points

$$\{\omega_i, A_i, \phi_i\}_{i=1}^{n} \longrightarrow \left\{\hat{\omega}_j, \hat{A}_j, \hat{\phi}_j\right\}_{j=1}^{N} \tag{3}$$

Let us assume the desired points for resampling are logarithmically spaced on the interval $[\omega_{\min}, \omega_{\max}]$, such that

$$\hat{\omega}_j = \omega_{\min}\left(\frac{\omega_{\max}}{\omega_{\min}}\right)^{\frac{j-1}{N-1}} \ . \tag{4}$$

Noting that the complex impedance is related to amplitude and phase via $Z = A\exp(i\phi)$, we introduce the new functions $C_i \doteq \cos(\phi_i)$ and $S_i \doteq \sin(\phi_i)$.

$$\hat{A}_j = \texttt{spline}\left[\{A_i\}, \hat{\omega}_j\right] \tag{5}$$
$$\hat{C}_j = \texttt{spline}\left[\{C_i\}, \hat{\omega}_j\right] \tag{6}$$
$$\hat{S}_j = \texttt{spline}\left[\{S_i\}, \hat{\omega}_j\right] \tag{7}$$
$$\hat{\phi}_j = \texttt{atan2}\left[S_i, C_i\right] \tag{8}$$

Here, `spline` refers to any suitable spline interpolation routine, and `atan2` refers to the two-argument arctangent function that appears in most modern programming languages. Unlike ϕ, the functions C and S are continuous. Thus, splitting the phase into two components ensures no problems when the phase crosses zero or when it wraps at ± 180 degrees.

A.3 Rejected measurements

Three measurements were rejected based on the appearance of the ω-dependence of the $B\ell$ and mass-consistency curves. These three cases looked qualitatively different than the other measurements and, in particular, behaved poorly at low frequency. Specifically, the $B\ell$ curves were abnormal, as shown in Fig. 14, and more importantly there was no identifiable region of mass consistency, as shown in Fig. 15.

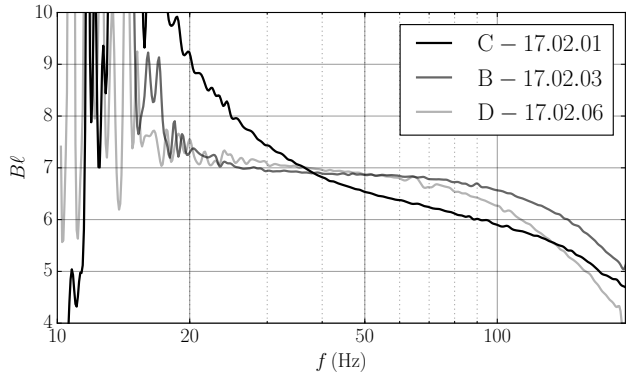

Fig. 14. Discarded data based on abnormally bad low-frequency behaviour. Compare with Fig. 5

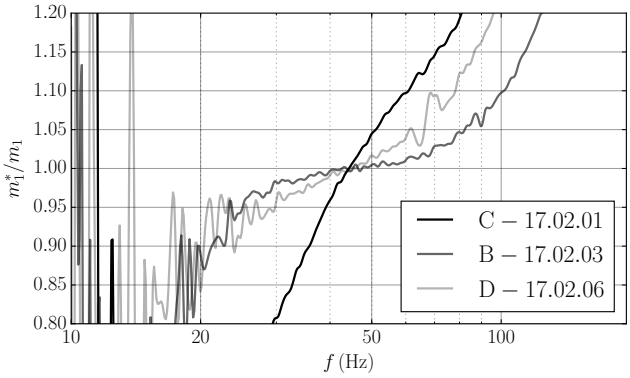

Fig. 15. Discarded data based on abnormally bad low-frequency behaviour and poor mass consistency. Compare with Fig. 8

The first measurement by C, dated 2017-02-01, was most clearly flawed case. Further tests indicated that the masses were attached near the surround, which means they are not fixed to the voice coil. This results in a dynamic contribution so that a flat $B\ell$ around f_s could not be identified.

A.4 Equivalent forms of the LOG model

It is possible to recast the expression for the LOG compliance in terms of logarithmic functions of arbitrary base and frequency normalization. Consider a LOG representation with frequency normalization ω_0, base b. Setting this equal to the LOG representation used in this paper gives

$$C_0\left[1-\lambda\log_b\left(\frac{i\omega}{\omega_0}\right)\right] = C\left[1-\beta\ln(i\omega)\right] . \tag{9}$$

The equality is exact, and some algebra shows that

$$C_0 = C\left(1-\beta\ln\omega_0\right) , \tag{10}$$

$$\lambda = \frac{\beta\ln b}{1-\beta\ln\omega_0} . \tag{11}$$

For example, if we choose $b = 10$ and $\omega_0 = \omega_s$ as in Eq. (5) of Ref. [9], then

$$C_0 = C\left(1-\beta\ln\omega_s\right) \quad \text{and} \quad \lambda = \frac{\beta\ln 10}{1-\beta\ln\omega_s} . \tag{12}$$

In the original paper by Knudsen and Jensen [5], $\omega_0 = 1$ and $b = 10$, so that the conversion requires

$$C_0 = C \quad \text{and} \quad \lambda = \beta\ln 10 . \tag{13}$$

THE AUTHORS

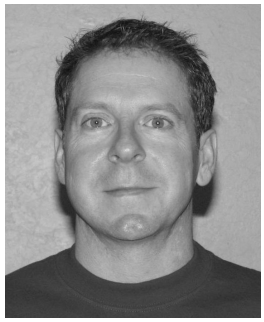

Jeff Candy

Claus Futtrup

Jeff Candy was born in Edmonton, Canada in 1966. He received his Ph.D. in Physics from the University of California, San Diego in 1994, and is currently manager of the Turbulence and Transport Group at General Atomics in San Diego, California. His research spans various topics in theoretical and computational plasma physics, with specific focus on plasma kinetic theory and turbulence. In the field of audio, he is interested in the application of methods in theoretical acoustics to practical situations. Dr. Candy is a member of the Audio Engineering Society and a fellow of the American Physical Society (APS). In 2003, he received the Rosenbluth Award for fusion theory, and was 2008 Jubileum Professor at Chalmers University.

●

Claus Futtrup was born in Herning, Denmark, in 1971. He received his M.Sc. in Mechanical Engineering in 1997 from Aalborg University. His specialization was material science: steel and other metals, ceramics, rubber, plastics, and composites in regard to design parameters, process engineering, and chemical and environmental issues. From 1997 to 2006 he worked at Dynaudio A/S in Skanderborg, Denmark, as an R&D Engineer, designing loudspeaker enclosures and finally as an automotive system engineer. From 2006, he was employed as a transducer design engineer at Tymphany Denmark and, in 2008, he became R&D manager at Scan-Speak. In September 2013, he became Technical Sales Manager at SEAS, Norway, and in March 2015 was promoted to CTO.